

## Enhanced Electroluminescence from a Thermally Activated Delayed-Fluorescence Emitter by Suppressing Nonradiative Decay

Katsuyuki Shizu,<sup>1,2,3</sup> Motoyuki Uejima,<sup>4</sup> Hiroko Nomura,<sup>1</sup> Tohru Sato,<sup>4,5</sup> Kazuyoshi Tanaka,<sup>4</sup> Hironori Kaji,<sup>2</sup> and Chihaya Adachi<sup>1,3,6</sup>

<sup>1</sup>Center for Organic Photonics and Electronics Research (OPERA),  
Kyushu University, 744 Motoooka, Nishi, Fukuoka 819-0395, Japan

<sup>2</sup>Institute for Chemical Research, Kyoto University, Uji, Kyoto 611-0011, Japan

<sup>3</sup>Japan Science and Technology Agency (JST), ERATO, Adachi Molecular Exciton Engineering Project,  
744 Motoooka, Nishi, Fukuoka 819-0395, Japan

<sup>4</sup>Department of Molecular Engineering, Graduate School of Engineering,  
Kyoto University, Kyoto 615-8510, Japan

<sup>5</sup>Unit of Elements Strategy Initiative for Catalysts and Batteries, Kyoto University, Kyoto 615-8510, Japan

<sup>6</sup>International Institute for Carbon Neutral Energy Research (WPI-I2CNER),  
Kyushu University, 744 Motoooka, Nishi, Fukuoka 819-0395, Japan

(Received 17 July 2014; revised manuscript received 12 November 2014; published 9 January 2015)

Thermally activated delayed-fluorescence (TADF) is a promising approach for realizing highly efficient organic light-emitting diodes (OLEDs). By controlling the spatial overlap between the frontier orbitals to suppress nonradiative decay, we develop a highly efficient TADF emitter,  $N^1$ -[4-(4,6-diphenyl-1,3,5-triazin-2-yl)phenyl]- $N^1$ -[4-(diphenylamino)-phenyl]- $N^4$ ,  $N^4$ -diphenylbenzene-1,4-diamine (DPA-TRZ). DPA-TRZ exhibits a photoluminescence quantum efficiency of 100% when doped into a host material, suggesting that nonradiative decay from its excited states is completely suppressed. Transient photoluminescence measurements confirm that DPA-TRZ emits TADF in a doped film. An OLED containing DPA-TRZ as a green emitter shows a maximum external quantum efficiency of 13.8%, which exceeds the theoretical limit for conventional fluorescent OLEDs. This high efficiency results from the effective generation of TADF and suppressed nonradiative decay in DPA-TRZ. Our molecular design strategy based on quantum chemistry provides a rational approach to control radiative and nonradiative decays for optimizing TADF materials.

DOI: 10.1103/PhysRevApplied.3.014001

### I. INTRODUCTION

Recently, it has been recognized that thermally activated delayed-fluorescence (TADF) is a promising pathway for converting triplet excitons into light, following our successive reports on highly efficient TADF [1–4]. In fact, the use of TADF compounds as emitters in organic light-emitting diodes (OLEDs) has resulted in highly efficient electroluminescence (EL). This marked improvement in EL efficiency means TADF emitters compete with phosphorescent ones [1]. Advantages of TADF compounds include not only high EL efficiency without rare metals, but also diversity of suitable chemical structures and ease of chemical modification [1–10].

Figure 1 shows an energy-level diagram for TADF, which involves two processes: conversion of the lowest triplet state ( $T_1$ ) to the lowest singlet excited state ( $S_1$ ) via reverse intersystem crossing (RISC), and radiative decay (fluorescence) from  $S_1$  to the ground state ( $S_0$ ). Nonradiative deactivation processes compete with RISC and fluorescence. Consequently, molecular design to improve the luminescence efficiency of TADF emitters requires: (1) a faster rate of  $S_1 \leftarrow T_1$  RISC than that of

competitive  $T_1 \rightarrow S_0$  nonradiative decay ( $k_{\text{RISC}} > k_{\text{nr}}'$ ); (2) a faster rate of  $S_1 \rightarrow S_0$  radiative decay than that of competitive  $S_1 \rightarrow S_0$  nonradiative decay ( $k_r > k_{\text{nr}}$ ). Therefore, suppressing nonradiative decay is crucial for improving the internal quantum efficiency of TADF compounds.

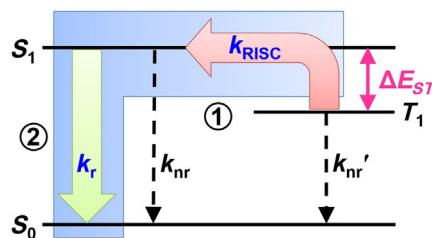


FIG. 1. Energy-level diagram for thermally activated delayed-fluorescence (TADF).  $S_0$  denotes the ground state.  $S_1$  and  $T_1$  denote the lowest excited singlet and lowest triplet states, respectively.  $k_{\text{RISC}}$  is the rate of reverse intersystem crossing from  $T_1$  to  $S_1$ ;  $k_{\text{nr}}'$  is the rate of nonradiative decay from  $T_1$  to  $S_0$ ;  $k_r$  is the rate of radiative decay from  $S_1$  to  $S_0$ ;  $k_{\text{nr}}$  is the rate of nonradiative decay from  $S_1$  to  $S_0$ .  $\Delta E_{ST}$  is the difference between the  $S_1$  and  $T_1$  energy levels.

A large  $k_{\text{RISC}}$  in a TADF compound can be realized by spatially separating its highest occupied molecular orbital (HOMO) and lowest unoccupied molecular orbital (LUMO) [1–10]. Because  $k_{\text{RISC}}$  is expressed as  $k_{\text{RISC}} \propto \exp(-\Delta E_{ST})$  [11,12], where  $\Delta E_{ST}$  is the energy difference between  $S_1$  and  $T_1$ ,  $k_{\text{RISC}}$  can be increased by decreasing  $\Delta E_{ST}$ . The spatial overlap between the HOMO and LUMO predominantly affects  $\Delta E_{ST}$  when the HOMO-LUMO transition makes a dominant contribution to  $S_1$  and  $T_1$ . In such cases,  $\Delta E_{ST}$  is approximately equal to  $2K$ , where  $K$  is the exchange integral between the HOMO and LUMO, and decreases with decreasing spatial overlap [13]. A small spatial overlap therefore results in a small  $\Delta E_{ST}$ , leading to a large  $k_{\text{RISC}}$ .

In contrast, a large  $k_r$  can be realized by increasing the spatial overlap between the HOMO and LUMO. Because  $k_r$  is expressed as  $k_r \propto |\boldsymbol{\mu}_{10}|^2$ , where  $\boldsymbol{\mu}_{10}$  is the transition dipole moment between  $S_0$  and  $S_1$  [14],  $k_r$  increases with increasing  $|\boldsymbol{\mu}_{10}|$ .  $|\boldsymbol{\mu}_{10}|$  can be expressed in terms of a three-dimensional function called transition dipole moment density  $\tau_{10}$  [15–17],

$$|\boldsymbol{\mu}_{10}| = \int \tau_{10}(\mathbf{x}) d\mathbf{x}, \quad (1)$$

where  $\mathbf{x}$  is a point in three-dimensional space. The origin of the coordinates is at the center of nuclear charges.  $\tau_{10}$  is related to the overlap density  $\rho_{10}$  between the electronic wave functions of  $S_0$  and  $S_1$  by the following equation [15]:

$$\tau_{10}(\mathbf{x}) = \rho_{10}(\mathbf{x})(-e\mathbf{x}) \cdot \frac{\boldsymbol{\mu}_{10}}{|\boldsymbol{\mu}_{10}|}, \quad (2)$$

where  $e$  is the elementary charge. According to Eqs. (1) and (2),  $\tau_{10}$  can be viewed as a density form for  $|\boldsymbol{\mu}_{10}|$  because the spatial integral of  $\tau_{10}$  gives  $|\boldsymbol{\mu}_{10}|$ . This relation is analogous to that holding for the electron density and number of electrons: the spatial integral of the electron density gives the number of electrons. The density map of  $\tau_{10}$  provides an interpretation of where an electronic transition occurs in a molecule. The elements of  $\mathbf{x}$  increase with increasing distance from the origin. Therefore, when  $\rho_{10}$  is widely distributed, at least one of the elements of  $\rho_{10} \times (-e\mathbf{x})$  has a large value at points distant from the origin, and the resultant  $\tau_{10}$  is large. Such wide  $\rho_{10}$  distributions can be realized by increasing spatial overlap between the wave functions of  $S_0$  and  $S_1$ . When the HOMO-LUMO transition dominates  $S_0$ - $S_1$  transition,  $\rho_{10}$  is approximately equal to the spatial overlap between the HOMO and LUMO. Hence, a large  $|\boldsymbol{\mu}_{10}|$  can be realized by increasing the HOMO-LUMO spatial overlap. However, as mentioned above, a large overlap generally induces large  $\Delta E_{ST}$  and reduces  $k_{\text{RISC}}$ , which inhibits the efficient generation of TADF. As a result, it is necessary to modulate the trade-off between  $\Delta E_{ST}$  and  $|\boldsymbol{\mu}_{10}|$  by adjusting  $\rho_{10}$  to enhance the luminescence efficiency of TADF compounds.

$k_{\text{nr}}$  also increases when the spatial overlap between the HOMO and LUMO is increased. Because  $k_{\text{nr}}$  can be approximately expressed in terms of the vibronic coupling constant  $V_{10}^m$  and the  $S_0$ - $S_1$  excitation energy  $\Delta E_{10}$  as  $\sum_m (V_{10}^m)^2 / (\Delta E_{10})^2$  [18],  $k_{\text{nr}}$  increases with increasing  $V_{10}^m$ .  $V_{10}^m$  measures the magnitude of the intramolecular vibronic coupling caused by the  $m$ th intramolecular vibrational mode. Intramolecular vibronic coupling is an origin of  $S_1 \rightarrow S_0$  nonradiative decay in an emitting molecule. As with  $|\boldsymbol{\mu}_{10}|$ ,  $V_{10}^m$  can be expressed in terms of  $\rho_{10}$  [15],

$$V_{10}^m(\mathbf{x}) = \int \rho_{10}(\mathbf{x}) \left( -\sum_A \frac{Z_A}{\sqrt{M_A}} \mathbf{e}_A^{(m)} \cdot \frac{\mathbf{x} - \mathbf{R}_A}{|\mathbf{x} - \mathbf{R}_A|} \right) d\mathbf{x}, \quad (3)$$

where  $Z_A$ ,  $M_A$ , and  $\mathbf{R}_A$  are the charge, mass, and position of the  $A$ th nucleus, respectively.  $\mathbf{e}_A^{(m)}$  is a three-dimensional

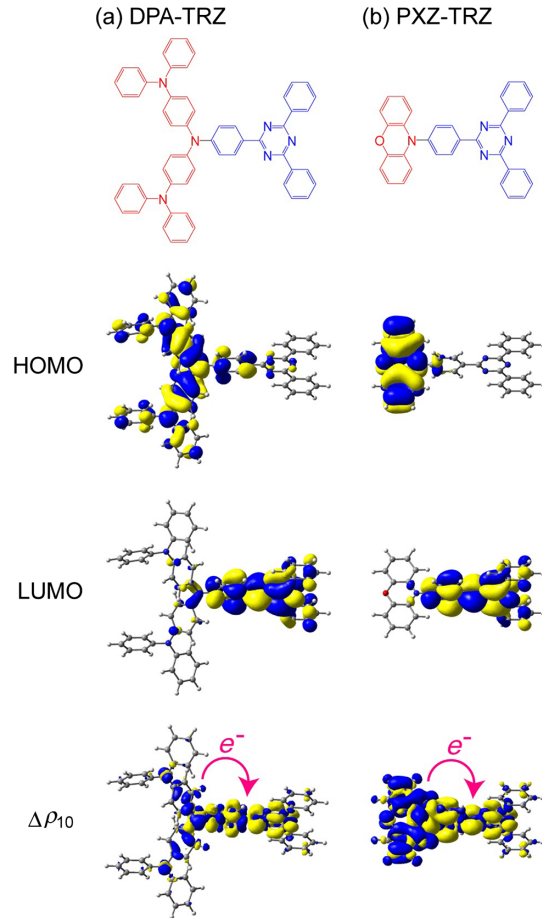


FIG. 2. Chemical structures and isosurfaces for the HOMO, LUMO, and electron-density difference  $\Delta\rho_{10}$  associated with the  $S_1 \leftarrow S_0$  excitation of (a) DPA-TRZ and (b) PXZ-TRZ calculated at the TD-M06-2X-cc-pVDZ level of theory. Donor and acceptor moieties are shown in red and blue, respectively. Isosurface values for the HOMO, LUMO, and  $\Delta\rho_{10}$  of DPA-TRZ and PXZ-TRZ are 0.02, 0.02, and 0.001 a.u., respectively (yellow regions, positive; blue regions, negative).

vector and represents the relative displacement of the  $A_{th}$  nucleus for the  $m$ th vibrational mode. Equation (3) shows that  $V_{10}^m$  increases with increasing  $\rho_{10}$ ; in other words, with increasing spatial overlap between the HOMO and LUMO. Increasing this spatial overlap therefore generally increases both  $k_r$  and  $k_{nr}$ . Equation (3) shows that intramolecular vibronic couplings can be suppressed by controlling  $\rho_{10}$  distribution [16,17].

By controlling the HOMO and LUMO distributions and the resultant spatial overlap between them, we can suppress nonradiative decay in TADF compounds and improve their photoluminescence quantum yields (PLQYs). Comparing Eqs. (1) and (2) shows that the dependence of  $|\mu_{10}|$  on  $\rho_{10}$  is different from that of  $V_{10}^m$ . By utilizing the difference between them, we can design a TADF compound with large  $|\mu_{10}|$  and small  $V_{10}^m$  that exhibits high PLQY. This study focuses on the molecular design of a TADF compound that achieves high PLQY by controlling the spatial overlap between HOMO and LUMO and suppressing nonradiative decay. The TADF compound  $N^1$ -[4-(4,6-diphenyl-1,3,5-triazin-2-yl)phenyl]- $N^1$ -[4-(diphenylamino)-phenyl]- $N^4$ ,  $N^4$ -diphenylbenzene-1,4-diamine (denoted DPA-TRZ; see Fig. 2) is designed to exhibit weaker nonradiative decay and higher luminescence efficiency than previously reported 10-[4-(4,6-diphenyl-1,3,5-triazin-2-yl)phenyl]-10*H*-phenoxazine (PXZ-TRZ) [7], by changing its electron-donating moiety. When doped into a host material, DPA-TRZ exhibits a PLQY of 100%, suggesting that nonradiative decay is completely suppressed in this molecule. An OLED using DPA-TRZ as an emitter shows a maximum external quantum efficiency (EQE) of 13.8%, which is higher than that obtained using PXZ-TRZ.

## II. EXPERIMENTAL METHODS

Synthesis and characterization data for DPA-TRZ are shown in the Supplemental Material (SM) [19]. NMR spectra used in the characterization of products were recorded on a Bruker Biospin Avance-III 500 NMR spectrometer at ambient temperature. All NMR spectra were referenced to solvent. Matrix-assisted laser desorption/ionization (MALDI) time-of-flight (TOF) mass spectrometries (MS) were recorded on a Bruker Daltonics Autoflex III spectrometer using positive mode. UV-visible and photoluminescence (PL) spectra were measured using a UV-visible spectrophotometer (UV-2550, Shimadzu, Japan) and spectrofluorometer (Fluoromax-4, Horiba Jobin Yvon), respectively. PLQYs were measured using an absolute PLQY spectrometer (C11347 Quantaurus-QY, Hamamatsu Photonics, Japan). Time-resolved PL decays were measured using a fluorescence lifetime spectrometer (C11367 Quantaurus-tau, Hamamatsu Photonics, Japan). A yttrium-aluminum-garnet laser with a wavelength of 355 nm (LS-2132, LOTIS TII, Belarus) was used as an excitation source.

## III. RESULTS AND DISCUSSION

Time-dependent density functional theory [20,21] (TD-DFT) with the M06-2X functional [22] and correlation-consistent polarized valence double-zeta (cc-pVDZ) basis set [23] (denoted TD-M06-2X-cc-pVDZ) well describes  $S_1$  of DPA-TRZ. By taking into account the effect of solvent with the polarizable continuum model [24–26], the TD-M06-2X-cc-pVDZ method reasonably reproduces the experimental absorption and emission wavelengths of DPA-TRZ in toluene solution (see SM [19], Table S1). To calculate excited states of TADF compounds in solution, M06-2X and range-corrected functionals such as Coulomb-attenuated method based on the Becke three-parameter Lee-Yang-Parr (CAM-B3LYP) functional and  $\omega$ B97X-D perform well. In contrast, standard functionals without range correction, including B3LYP and PBE0 (where PBE is Perdew-Burke-Ernzerhof) tend to considerably underestimate emission wavelengths [1]. The electronic structures are calculated using the GAUSSIAN09 program package [27].

Detailed analysis based on quantum chemistry is made for isolated DPA-TRZ and PXZ-TRZ molecules. The calculations of excited states at the TD-M06-2X-cc-pVDZ level show that  $S_1$  of DPA-TRZ and PXZ-TRZ have charge-transfer (CT) character.  $S_1$  of DPA-TRZ corresponds to CT from the donor to the acceptor moieties: the electronic transition between spatially separated HOMO and LUMO is dominant [Fig. 2(a) and SM [19], Table S2]. The calculated electron-density difference  $\Delta\rho_{10}$  associated with the  $S_1 \leftarrow S_0$  excitation shows that electron transfer occurs from donor to acceptor moieties:  $\Delta\rho_{10}$  decreases in the donor moiety (blue region), and increases in the acceptor moiety (yellow region). Electronic configurations with configuration interaction (CI) coefficients larger than  $1.0 \times 10^{-4}$  are included in the calculation of  $\Delta\rho_{10}$ . The room-temperature absorption and emission spectra of DPA-TRZ in toluene solution are reported in SM [19], Fig. S1. The observation of broad absorption and emission bands indicates that  $S_1$  of DPA-TRZ is of CT character. The calculations for PXZ-TRZ show that its  $S_1$  also has CT character. The calculated  $\Delta\rho_{10}$  shows that in  $S_1 \leftarrow S_0$  excitation, electron transfer occurs from the donor to acceptor moieties.

The nonradiative decay of DPA-TRZ in toluene solution is suppressed more than that of PXZ-TRZ. The PLQY of DPA-TRZ in toluene solution ( $10^{-5}M$ ) measured in air is 35%. The excitation wavelength is 330 nm. After  $N_2$  bubbling for 5 min to exclude  $O_2$  (a triplet quencher), the PLQY increases to 45%, suggesting that  $O_2$ -sensitive triplet states are involved in the PL, and TADF via  $S_1 \leftarrow T_1$  RISC is observed. These PLQY values are higher than those of PXZ-TRZ (in air: 15%; after excluding  $O_2$ : 29%) [7]. Therefore, we conclude that nonradiative decay is suppressed more in DPA-TRZ than in PXZ-TRZ.

Quantum-chemical calculations suggest that DPA-TRZ shows a higher PLQY than PXZ-TRZ because DPA-TRZ

has a larger  $|\mu_{10}|$ , so  $S_1 \rightarrow S_0$  nonradiative decay is better suppressed in DPA-TRZ than in PXZ-TRZ.  $|\mu_{10}|$  of DPA-TRZ and PXZ-TRZ calculated at the TD-M06-2X-cc-pVDZ level are  $3.38$  and  $2.26 \times 10^{-4}$  a.u., respectively, so  $|\mu_{10}|$  of DPA-TRZ is approximately  $10^4$  times larger than that of PXZ-TRZ. Unlike  $|\mu_{10}|$ ,  $V_{10}^m$  calculated for DPA-TRZ and PXZ-TRZ are comparable: the maximum  $V_{10}^m$  of DPA-TRZ is less than 10 times that of PXZ-TRZ (Fig. 3). The calculations suggest that the difference between  $k_r$  and  $k_{nr}$  is larger for DPA-TRZ than for PXZ-TRZ. Consequently, nonradiative decay is suppressed more effectively in DPA-TRZ than in PXZ-TRZ, so DPA-TRZ has a higher PLQY than PXZ-TRZ.

The large  $|\mu_{10}|$  of DPA-TRZ originates from its large  $\tau_{10}$  distribution caused by the large spatial overlap between HOMO and LUMO. Figure 4 shows calculated  $\rho_{10}$  and  $\tau_{10}$  for DPA-TRZ and PXZ-TRZ. Electronic configurations with CI coefficients larger than  $1.0 \times 10^{-4}$  are included in these calculations. For DPA-TRZ,  $\rho_{10}$  extends over the entire molecule, and the resultant  $\tau_{10}$  is large, leading to a large  $|\mu_{10}|$ . For PXZ-TRZ,  $\rho_{10}$  and  $\tau_{10}$  are predominantly localized on the phenoxazine moiety. In addition, positive and negative regions are almost symmetrically distributed.  $|\mu_{10}|$  (the spatial integral of  $\tau_{10}$ ) is therefore small compared with that of DPA-TRZ. The distribution pattern of  $\rho_{10}$  reflects the spatial overlap between HOMO and LUMO

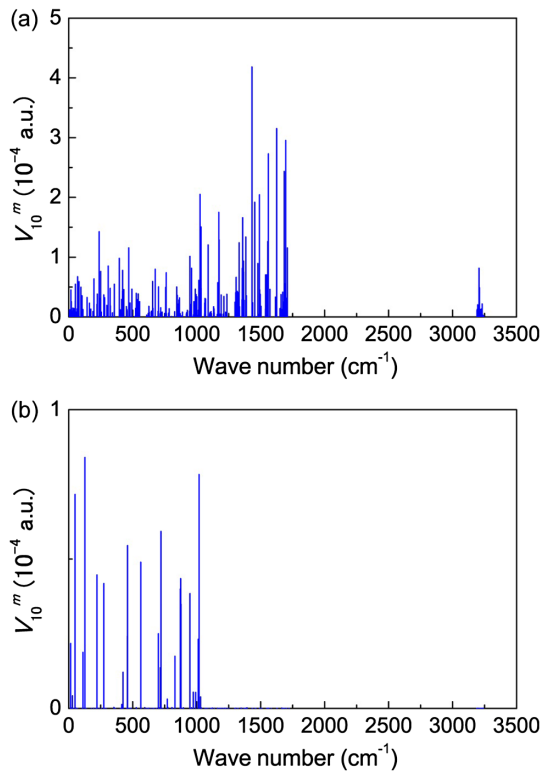


FIG. 3. Vibronic coupling constants  $V_{10}^m$  (in atomic units) of (a) DPA-TRZ and (b) PXZ-TRZ calculated at the TD-M06-2X-cc-pVDZ level of theory.

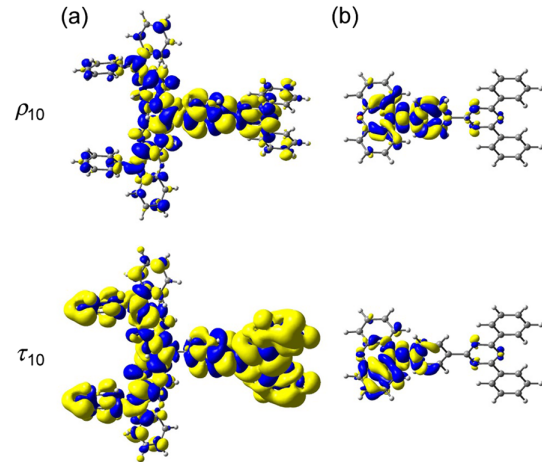


FIG. 4. Overlap densities  $\rho_{10}$  and transition dipole moment densities  $\tau_{10}$  of (a) DPA-TRZ and (b) PXZ-TRZ calculated at the TD-M06-2X-cc-pVDZ level of theory. Isosurface values for  $\rho_{10}$  and  $\tau_{10}$  of DPA-TRZ and PXZ-TRZ are  $0.0004$  and  $0.001$  a.u., respectively (yellow regions, positive; blue regions, negative).

because the HOMO-LUMO transition is dominant for  $S_1$  of these two molecules. The large  $\rho_{10}$ ,  $\tau_{10}$ , and  $|\mu_{10}|$  of DPA-TRZ originate from the considerable spatial overlap between its HOMO and LUMO. We can thus qualitatively understand the origin of the relative magnitudes of  $|\mu_{10}|$  of DPA-TRZ and PXZ-TRZ by comparing  $\rho_{10}$  and  $\tau_{10}$  distributions.

When doped into a host material, nonradiative decay of DPA-TRZ is completely suppressed. A 6 wt % DPA-TRZ-doped 9,9'-biphenyl-3,3'-diylbis-9H-carbazole (mCBP) film was prepared by codeposition under vacuum. The inset in Fig. 5 shows a PL spectrum of the doped film measured at 300 K. The excitation wavelength is 325 nm. The PL spectrum shows a single broad peak (540 nm) corresponding to the  $S_0$ - $S_1$  transition in DPA-TRZ. The PLQY reaches nearly 100%, suggesting that excitons generated on the mCBP host are completely transferred

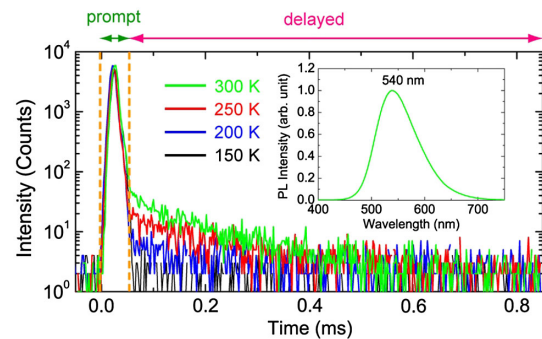


FIG. 5. Transient photoluminescence decays for a 6 wt % DPA-TRZ:mCBP film measured at temperatures of 150 to 300 K. The inset is a photoluminescence spectrum of the doped film measured at 300 K.

to DPA-TRZ and converted into light. In other words, nonradiative decay is completely suppressed. In contrast, nonradiative decay is not sufficiently suppressed for PXZ-TRZ. The PLQY of a 6 wt % PXZ-TRZ-doped CBP film is 65%; that is, 35% of excitons decays nonradiatively [7]. The PLQY of DPA-TRZ in the mCBP host is significantly high compared with that in the toluene solution. This is probably because structural deformation causing non-radiative decays are more suppressed in the solid-state mCBP host.

The transient PL characteristics of the doped film confirm that DPA-TRZ emits TADF (Fig. 5). The intense emission is assigned to prompt fluorescence because no intensity changes are observed in the 150–300 K range. The long tails are assigned to TADF (delayed component) because their intensity increases with temperature. At 300 K, the lifetime of the delayed component is 160  $\mu$ s. From the observed photon counts, we estimate the contributions from prompt and delayed fluorescence to the total PLQY of DPA-TRZ. At 300 K, the prompt component accounts for 92.9% of the total PLQY, reflecting the fast radiative decay (the large  $|\mu_{10}|$ ) of DPA-TRZ. The remaining 7.1% of excitons are converted into light via TADF. From peak maxima of fluorescence and phosphorescence spectra of the doped film measured at 10 K (see SM [19], Fig. S2), the  $S_1$  and  $T_1$  energies of DPA-TRZ are estimated to be 2.30 eV (540 nm) and 2.19 eV (566 nm), respectively. Therefore,  $\Delta E_{ST}$  is determined to be 0.11 eV, which is sufficiently small to generate TADF. The  $S_1$  and  $T_1$  energies of PXZ-TRZ-doped mCBP film are 2.30 eV (540 nm) and 2.23 eV (556 nm), respectively, and the resultant  $\Delta E_{ST}$  is 0.07 eV [27]. Although the  $S_1$  energies are equivalent, because the  $T_1$  energy of DPA-TRZ is lower than that of PXZ-TRZ, the  $\Delta E_{ST}$  is larger for DPA-TRZ than for PXZ-TRZ.

Figure 6 shows proposed exciton generation and decay processes in DPA-TRZ. For the PL process, (a) excitation

of  $S_0$  results in the production of  $S_1$  excitons. (b) Of these  $S_1$  excitons, 92.9% decay radiatively ( $S_1 \rightarrow S_0$ ), and the remaining 7.1% are converted into  $T_1$  excitons via inter-system crossing (ISC) ( $S_1 \rightarrow T_1$ ). (c)  $S_1$  excitons are formed from  $T_1$  excitons via RISC ( $S_1 \leftarrow T_1$ ). Finally, the  $S_1$  excitons decay radiatively ( $S_1 \rightarrow S_0$ ). In these processes, the competitive nonradiative decay pathways are completely suppressed. For the EL process, (d) charge recombination in the host material produces  $S_1$  and  $T_1$  excitons with a 1:3 ratio; i.e., 25%  $S_1$  excitons and 75%  $T_1$  excitons. (e) Out of the 25% of  $S_1$  excitons, 92.9% (23.2% of the total excitons) decay radiatively ( $S_1 \rightarrow S_0$ ), and the remaining 7.2% (1.8% of the total excitons) are converted into  $T_1$  excitons via ISC ( $S_1 \rightarrow T_1$ ). (f) Finally, the resultant 76.8% (75% + 1.8%) of  $T_1$  excitons are converted into light as TADF.

To evaluate the ability of DPA-TRZ as an emitter for OLEDs, an OLED with a configuration of indium tin oxide (ITO) (100 nm)– $N,N'$ -diphenyl- $N,N'$ -bis(1-naphthyl)-1,10-biphenyl-4-4'-diamine ( $\alpha$ -NPD) (35 nm)–6 wt %-DPA-TRZ:mCBP (15 nm)–TPBi (65 nm)–LiF (0.8 nm)–Al (100 nm) was fabricated by vacuum deposition. In the Supplemental Material [19], Fig. S3 shows the EQE and current density characteristics of this OLED, and its EL spectrum at a current density of 100 mA cm<sup>-2</sup>. The EQEs at low current densities surpass the theoretical maximum EQE (5%) of conventional fluorescent OLEDs: EQEs are 13.8%, 11.2%, and 7.9% at current densities of 0.01, 0.1, and 1 mA cm<sup>-2</sup>, respectively. The maximum EQE of 13.8% is higher than that obtained with PXZ-TRZ (12.5%). The OLED exhibits green emission with a maximum at 548 nm resulting from the  $S_1 \rightarrow S_0$  radiative decay of DPA-TRZ. We have, therefore, successfully improved the efficiency of a TADF-based OLED by changing the donor moiety of PXZ-TRZ and suppressing nonradiative decay. We note that comprehensive optimization of the OLED device architecture will lead to 100% internal efficiency because DPA-TRZ intrinsically has 100% fluorescence and RISC efficiencies. The EL efficiency can be improved, for example, by changing the host material. In fact, the EL efficiency of OLEDs containing TADF emitter 1,2,3,5-tetrakis(carbazol-9-yl)-4,6-dicyanobenzene (4CzIPN) has been increased over 20% by using various host materials and mixed host structures [28,29]. Further optimization will be reported in a successive study. The contributions from the prompt and delayed components of DPA-TRZ to the maximum EQE are calculated to be 3.2% and 10.6%, respectively (the calculation of the contributions are reported elsewhere [9]). This suggests that if DPA-TRZ is a conventional fluorescent emitter and does not emit TADF, the maximum EQE of its OLEDs is only 3.2%. TADF thus makes a marked contribution to the overall EQE and is responsible for the high EL efficiency of the OLED containing DPA-TRZ.

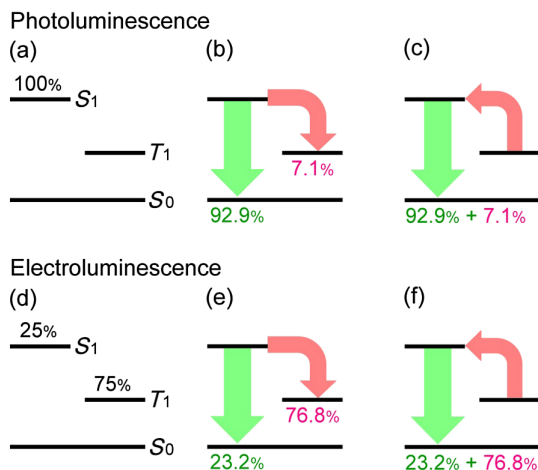


FIG. 6. Exciton generation and decay processes for (a)–(c) photoluminescence and (d)–(f) electroluminescence.

#### IV. SUMMARY

By controlling radiative and nonradiative decay through careful modulation of the overlap between HOMO and LUMO, we successfully develop a highly efficient TADF emitter, DPA-TRZ. Nonradiative decay of DPA-TRZ in an mCBP host is completely suppressed. An OLED containing DPA-TRZ as a green emitter exhibits a maximum EQE of 13.8%, which exceeds efficiencies obtained with conventional fluorescent emitters. This high efficiency results from generation of TADF and suppressed nonradiative decay in DPA-TRZ. We theoretically justify our rational approach to control radiative and nonradiative decays and we use it to optimize TADF materials.

#### ACKNOWLEDGMENTS

This research was funded by the Japan Society for the Promotion of Science (JSPS) through the “Funding Program for World-Leading Innovative R&D on Science and technology (FIRST Program).” The authors thank Kensuke Masui (Fujifilm Corporation, Tokyo, Japan) for his contribution to the analysis of photoluminescence and electroluminescence characteristics. The computation was partly carried out using the computer facilities at the Research Institute for Information Technology, Kyushu University, and the Academic Center for Computing and Media Studies (ACCMS), Kyoto University.

- 
- [1] H. Uoyama, K. Goushi, K. Shizu, H. Nomura, and C. Adachi, Highly efficient organic light-emitting diodes from delayed fluorescence, *Nature (London)* **492**, 234 (2012).
- [2] Q. Zhang, J. Li, K. Shizu, S. Huang, S. Hirata, H. Miyazaki, and C. Adachi, Design of efficient thermally activated delayed fluorescence materials for pure blue organic light emitting diodes, *J. Am. Chem. Soc.* **134**, 14706 (2012).
- [3] K. Sato, K. Shizu, K. Yoshimura, A. Kawada, H. Miyazaki, and C. Adachi, Organic luminescent molecule with energetically equivalent singlet and triplet excited states for organic light-emitting diodes, *Phys. Rev. Lett.* **110**, 247401 (2013).
- [4] Q. Zhang, B. Li, S. Huang, H. Nomura, H. Tanaka, and C. Adachi, Efficient blue organic light-emitting diodes employing thermally activated delayed fluorescence, *Nat. Photonics* **8**, 326 (2014).
- [5] T. Nakagawa, S.-Y. Ku, K.-T. Wong, and C. Adachi, Electroluminescence based on thermally activated delayed fluorescence generated by a spirobifluorene donor-acceptor structure, *Chem. Commun. (Cambridge)* **48**, 9580 (2012).
- [6] G. Méhes, H. Nomura, Q. Zhang, T. Nakagawa, and C. Adachi, Enhanced electroluminescence efficiency in a spiro-acridine derivative through thermally activated delayed fluorescence, *Angew. Chem., Int. Ed. Engl.* **51**, 11311 (2012).
- [7] H. Tanaka, K. Shizu, H. Miyazaki, and C. Adachi, Efficient green thermally activated delayed fluorescence (TADF) from a phenoxazine-triphenyltriazine (PXZ-TRZ) derivative, *Chem. Commun. (Cambridge)* **48**, 11392 (2012).
- [8] H. Tanaka, K. Shizu, H. Nakanotani, and C. Adachi, Twisted intramolecular charge transfer state for long-wavelength thermally activated delayed fluorescence, *Chem. Mater.* **25**, 3766 (2013).
- [9] J. Lee, K. Shizu, H. Tanaka, H. Nomura, T. Yasuda, and C. Adachi, Oxadiazole- and triazole-based highly-efficient thermally activated delayed fluorescence emitters for organic light-emitting diodes, *J. Mater. Chem. C* **1**, 4599 (2013).
- [10] K. Nasu, T. Nakagawa, H. Nomura, C.-J. Lin, C.-H. Cheng, M.-R. Tseng, T. Yasuda, and C. Adachi, A highly luminescent spiro-anthracenone-based organic light-emitting diode exhibiting thermally activated delayed fluorescence, *Chem. Commun. (Cambridge)* **49**, 10385 (2013).
- [11] J. C. Fister and J. M. Harris, Time- and wavelength-resolved delayed-fluorescence emission from acridine yellow in an inhomogeneous saccharide glass, *Anal. Chem.* **68**, 639 (1996).
- [12] M. N. Berberan-Santos and J. M. M. Garcia, Unusually strong delayed fluorescence of C70, *J. Am. Chem. Soc.* **118**, 9391 (1996).
- [13] N. J. Turro, V. Ramamurthy, and J. C. Scaiano, *Modern Molecular Photochemistry of Organic Molecules* (University Science Books, Sausalito, 2010).
- [14] D. Topygin, Effects of the solvent refractive index and its dispersion on the radiative decay rate and extinction coefficient of a fluorescent solute, *J. Fluoresc.* **13**, 201 (2003).
- [15] T. Sato, M. Uejima, N. Iwahara, N. Haruta, K. Shizu, and K. Tanaka, Vibronic coupling density and related concepts, *J. Phys. Conf. Ser.* **428**, 012010 (2013).
- [16] M. Uejima, T. Sato, K. Tanaka, and H. Kaji, Enhancement of fluorescence in anthracene by chlorination: Vibronic coupling and transition dipole moment density analysis, *Chem. Phys.* **430**, 47 (2014).
- [17] M. Uejima, T. Sato, M. Detani, A. Wakamiya, F. Suzuki, H. Suzuki, T. Fukushima, K. Tanaka, Y. Murata, C. Adachi, and H. Kaji, A designed fluorescent anthracene derivative: Theory, calculation, synthesis, and characterization, *Chem. Phys. Lett.* **602**, 80 (2014).
- [18] S. Manzhos, H. Segawa, and K. Yamashita, A model for recombination in Type II dye-sensitized solar cells: Catechol-thiophene dyes, *Chem. Phys. Lett.* **504**, 230 (2011).
- [19] See Supplemental Material at <http://link.aps.org/supplemental/10.1103/PhysRevApplied.3.014001> for synthesis, characterization data, quantum-chemical calculations, photophysical properties, and OLED characteristics for DPA-TRZ.
- [20] R. Bauernschmitt and R. Ahlrichs, Treatment of electronic excitations within the adiabatic approximation of time dependent density functional theory, *Chem. Phys. Lett.* **256**, 454 (1996).
- [21] M. E. Casida, C. Jamorski, K. C. Casida, and D. R. Salahub, Molecular excitation energies to high-lying bound states from time-dependent density-functional response theory: Characterization and correction of the time-dependent local density approximation ionization threshold, *J. Chem. Phys.* **108**, 4439 (1998).

- [22] Y. Zhao and D. Truhlar, The M06 suite of density functionals for main group thermochemistry, thermochemical kinetics, noncovalent interactions, excited states, and transition elements: Two new functionals and systematic testing of four M06-class functionals and 12 other functionals, *Theor. Chem. Acc.* **120**, 215 (2008).
- [23] J. T. H. Dunning, Gaussian basis sets for use in correlated molecular calculations. I. The atoms boron through neon and hydrogen, *J. Chem. Phys.* **90**, 1007 (1989).
- [24] J. Tomasi, B. Mennucci, and R. Cammi, Quantum mechanical continuum solvation models, *Chem. Rev.* **105**, 2999 (2005).
- [25] R. Improta, V. Barone, G. Scalmani, and M. J. Frisch, A state-specific polarizable continuum model time dependent density functional theory method for excited state calculations in solution, *J. Chem. Phys.* **125**, 054103 (2006).
- [26] R. Improta, G. Scalmani, M. J. Frisch, and V. Barone, Toward effective and reliable fluorescence energies in solution by a new state specific polarizable continuum model time dependent density functional theory approach, *J. Chem. Phys.* **127**, 074504 (2007).
- [27] M. J. Frisch *et al.*, *GAUSSIAN 09, Revision C.01* (Gaussian, Inc., Wallingford, CT, 2009).
- [28] B. S. Kim and J. Y. Lee, Engineering of mixed host for high external quantum efficiency above 25% in green thermally activated delayed fluorescence device, *Adv. Funct. Mater.* **24**, 3970 (2014).
- [29] Y. J. Cho, K. S. Yook, and J. Y. Lee, A universal host material for high external quantum efficiency close to 25% and long lifetime in green fluorescent and Phosphorescent OLEDs, *Adv. Mater.* **26**, 4050 (2014).